Title:

Quantitative characterization of local deformation-fracture behavior in ferrite-martensite dual-phase steels with different martensite distributions

Authors:

Myeong-heom Park[1,*], Ryota Matsubayashi[1], Akinobu Shibata[1,2], Nobuhiro Tsuji[1,3,*]

Affiliation:

[1] Department of Materials Science and Engineering, Kyoto University, Yoshida Honmachi, Sakyo-ku, Kyoto 606-8501, Japan

[2] Research Center for Structural Materials, National Institute for Materials Science (NIMS), 1-2-1 Sengen, Tsukuba, 305-0047, Japan

[3] Elements Strategy Initiative for Structural Materials (ESISM), Kyoto University, Yoshida Honmachi, Sakyo-ku, Kyoto 606-8501, Japan

Contact:

*Corresponding author:

Email: park.myeongheom.8r@kyoto-u.ac.jp (Myeong-heom Park)

nobuhiro-tsuji@mtl.kyoto-u.ac.jp (Nobuhiro Tsuji)

Keywords: dual-phase steel; mechanical properties; digital image correlation (DIC); strain distribution; martensite morphology; micro-void.

Abstract

Low-carbon dual-phase (DP) steels, composed of a soft ferrite phase and a hard martensite phase, are known as promising advanced high-strength steels (AHSSs) due to their high strength and good ductility at low fabrication cost. However, the deformation behavior of DP steels is still not fully understood because of their complex mixed-phase distribution and mechanical interactions between two phases during deformation. The present study quantitatively investigated the effect of martensite distribution on mechanical properties and local deformation-fracture behavior, using the digital image correlation (DIC) technique. Two types of DP structures were prepared: one with a chained martensite distribution (chained DP) and one with an isolated martensite distribution (isolated DP). The chained DP specimen exhibited a superior tensile property, achieving both high strength and large ductility compared to the isolated DP specimen. DIC strain analysis revealed that the chained DP structure showed relatively homogeneous deformation due to the greater contribution of martensite to plastic deformation. In contrast, the isolated DP specimen experienced significant strain localization in the soft ferrite grains. Despite high global strains, non-plastically deformed zones were observed in the central regions of large, isolated martensite particles. Notable differences in micro-void evolution were also observed between the two specimens. The chained DP specimen had a large number of randomly distributed micro-voids, ranging from 0.5 μm to 2 μm in size. In contrast, the isolated DP specimen contained fewer micro-voids, with some aligned at an angle of ~65° to the tensile direction, potentially leading to early tensile fracture.

1. Introduction

The demand for high-strength steel has been increasing to enhance energy efficiency through the weight reduction of automotive components and related applications. Low-carbon dual-phase (DP) steel, composed of soft ferrite and hard martensite phases, has been widely used as an advanced high-strength steel (AHSS) due to its excellent strength-ductility balance at low production cost [1-4]. Additionally, its relatively low yield ratio (i.e., the value of yield strength/tensile strength) and good deformability at room temperature are attractive advantages for metal-forming manufacturing [5-6]. Another notable characteristic of DP steels is the easy controllability of mechanical properties by changing microstructural factors such as phase fraction, grain size, phase hardness and morphologies [1, 7-13]. Higher strength can be achieved by increasing either martensite fraction or martensite strength (hardness) [13]. This would roughly be understood based on the rule-of-mixture expressed as $\boldsymbol{\sigma} = \mathbf{f_F}\boldsymbol{\sigma_F} + \mathbf{f_M}\boldsymbol{\sigma_M}$ where $\boldsymbol{\sigma}$ and $\mathbf{f}$ denote stress and phase volume fraction, respectively, and subscripts $\mathbf{F}$ and $\mathbf{M}$ are ferrite and martensite, respectively. However, investigating the dependence of mechanical properties on morphology (distribution) was challenging because of a lack of detailed spatial information required for evaluating local deformation behavior.

The Digital image correlation (DIC) technique, which provides local strain distribution, is a powerful tool for characterizing the local deformation behavior of DP structure, and it has been applied to materials exhibiting a heterogeneous deformation [16-19]. Some previous studies [9, 10, 18] successfully obtained local strain maps of DP microstructure using the microscopic DIC (μ-DIC) technique, and they found that DP structures exhibited highly heterogeneous deformation with significant strain localization in soft ferrite grains. Terada et al. [9] reported that strain distribution is highly dependent on martensite distribution. They found that the DP structures with chained martensite exhibited relatively homogeneous deformation, compared to those with isolated martensite distributions. Similarly, Park et al. [10] also observed obvious differences in strain distribution between chained and isolated martensite distributions at 5% tensile strain, and they attempted to discuss global deformation-fracture behavior with micro-void evolution. On the other hand, despite successful reports of local deformation behavior in DP structures, the discussion of global ductility, including fracture behavior, has not progressed significantly due to the limited availability of systematic data on local strain evolution near the point of fracture. Surface degradation by heavy deformation or unexpected contaminations during tensile testing poses a technical obstacle for DIC analysis. Recently, this challenge has been overcome by additional pattern-making

approaches with nanoparticles or grid lines on the surface of microstructures [20-21]. Exhaustive strain analysis extending into the large deformation regime is believed to be crucial for fully understanding the global deformation and fracture behavior in DP structures [22-26].

The objective of the present study is to reveal the deformation-fracture characteristics of low-carbon DP structures with different martensite distributions. The study primarily focuses on analyzing local strain distribution in ferrite and martensite, as well as characterizing micro-void formation and growth. To achieve this, the study utilizes the DIC method in conjunction with careful microstructure observations throughout the entire deformation process, extending nearly up to tensile fracture. This integrated approach offers a comprehensive understanding of the deformation-fracture nature of DP structures, with a specific emphasis on how different martensite distributions influence their mechanical behavior.

2. Experimental procedure

2.1. Fabrication of DP structures with isolated and chained martensite distributions

A low-carbon steel with a chemical composition of Fe-2Mn-0.1C (Mn: 2.03, C: 0.099, Si: 0.01, P: <0.002, S: 0.001, Fe: Balanced; wt. %) was used in this study. The A_{e3} temperature, at which ferrite-austenite transformation occurred, was estimated to be 804℃ by Thermo Calc software, using TCFE7.0 thermodynamic database applicable to steels and Fe-based alloys. DP structures were obtained through intercritical annealing at the ferrite (α) + austenite (γ) two-phase region and subsequent water-quenching, leading to the transformation of austenite to martensite. It is known that the martensite distribution (morphology) in DP structure strongly depends on an initial microstructure or/and a heat treatment path (i.e., normal transformation (from γ to α) or reverse transformation (from α to γ)) prior to the intercritical annealing [7, 9, 10]. **Fig. 1** shows a schematic illustration of the Fe-C phase diagram and two kinds of representative heat treatment routes to obtain DP structures with different martensite distributions (morphology). In Route 1 of **Fig. 1**, where the specimen is firstly austenitized and then intercritically annealed, the ferrite forms preferentially along grain boundaries of the parent austenite phase, and the remaining austenite with an isolated shape transforms to martensite by water-quenching. The obtained DP structure having isolated martensite morphology will be referred to as "isolated DP structure", hereafter. In Route 2 of **Fig. 1**, where a low carbon ferrite-pearlite microstructure is intercritically annealed, the austenite preferentially forms along the grain boundary of ferrite or/and on a small portion of pearlite with a high carbon content, and this process obtains the DP structure having a chained martensite morphology, which will be referred to as "chained DP structure".

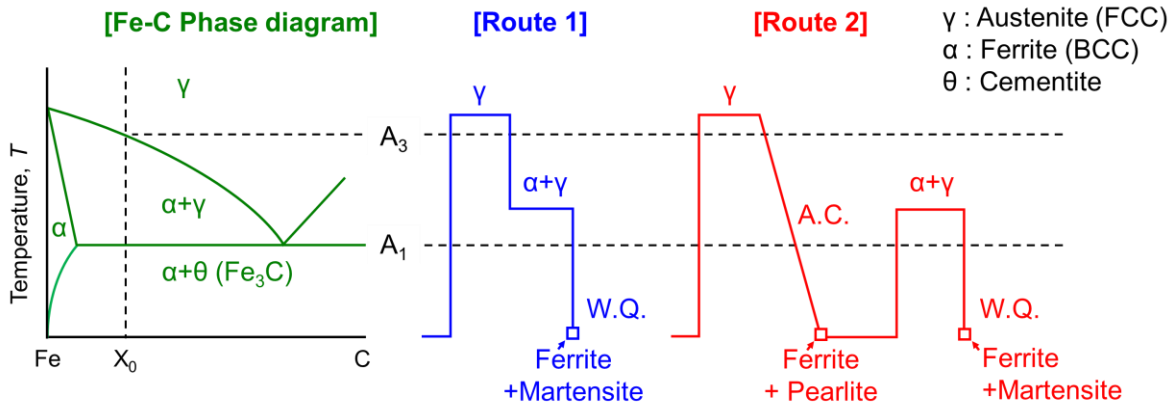


Fig. 1 Schematic illustration of the Fe-C phase diagram and two kinds of heat treatment routes to obtain DP structures with different martensite distributions.

Fig. 2 illustrates the heat treatment procedures used in the present study to fabricate the (a) isolated DP structure via Route 1 and (b) chained DP structure via Route 2. The A_{e3} temperature (804℃) was indicated by a gray solid line in **Fig. 2**. Initially, both routes underwent austenitizing heat treatment at 830℃ for 6 hr followed by water-quenching. Subsequently, three cycles of cyclic heat treatment were carried out at 810℃ for 3 minutes per cycle, with each cycle followed by water-quenching. These steps were performed to refine the austenite grains, as detailed in our previous papers [27, 28]. For the isolated DP structure, after the austenitizing and cycle heat treatment, the specimen was subjected to heat treatment at 810℃ for 3 minutes, then cooled down to 680℃ and held for 30 minutes in a salt bath, followed by water-quenching. This process is depicted by the blue line in **Fig. 2**(a). To obtain the chained DP specimen, the specimen was first heat-treated at 810℃ for 15 minutes and air-cooled to produce a ferrite + pearlite (F+P) structure. Subsequently, this F+P structured specimen underwent intercritical annealing for 740 ℃ for 30 minutes, followed by water-quenching. This process is represented by the red line in **Fig. 2**(b).

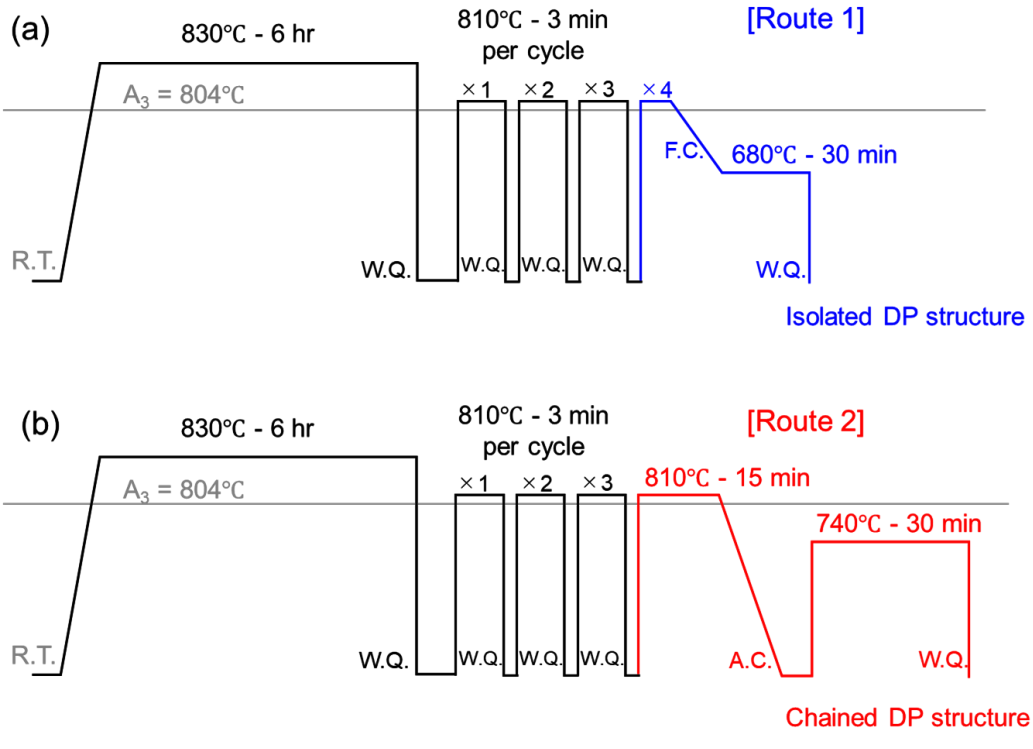


Fig. 2 Heat treatment schedules to obtain DP structures with (a) isolated martensite distribution and (b) chained martensite distributions in Fe-2Mn-0.1C low-carbon steels.

2.2. Microstructure observation

For the microstructure observation, specimens were mechanically polished with 400-4000 grit-sized sandpapers and then electrolytically polished with a solution of 10 vol. % $HClO_4$ and 90 vol. % CH_3COOH at a voltage of 20 V for 30 seconds at room temperature to obtain a flat mirror surface. Microstructures were characterized using field emission scanning electron microscopy (FE-SEM; JSM 7800F, JEOL) operated at an accelerating voltage of 15 kV, and a secondary electron (SE) imaging mode was employed for the observation. The average ferrite grain size in DP structures was measured by the line intercept method, and the martensite volume fraction was estimated by the pixel- and point-counting method on SEM images.

2.3. Tensile test and evaluation of local deformation behavior

The mechanical properties of DP structures were evaluated by a uniaxial tensile test with a quasi-static initial strain rate of 8.3×10^{-4} s^{-1} at room temperature, performed on a tensile testing machine (AG-100kN Xplus, Shimadzu) in displacement-controlled mode. The dog-bone-shaped tensile specimens having a gauge length of 10 mm, a gauge width of 5 mm and a thickness of 1 mm were prepared by electrical discharge machining, corresponding to 1/5 miniaturized size of the JIS (Japan Industrial Standard)-5 specimen. The specimen geometry is shown in **Fig. S1**(a) in the supplementary materials. The tensile strain was precisely measured by employing the digital image correlation (DIC) technique. The DIC technique was also used to investigate the local strain distribution of tensile-deformed specimens. The strain components, ε_{ij}, can be calculated, as follows:

$$\varepsilon_{ij} = \frac{1}{2}\left(\frac{\partial u_i}{\partial x_j} + \frac{\partial u_j}{\partial x_i}\right)$$

where, u_i, denotes displacement in the 2-dimensional axis. The von-Mises equivalent strain, ε_{eq}, was calculated using the following equation:

$$\varepsilon_{eq} = \sqrt{\frac{2}{3}\{(\varepsilon_1)^2 + (\varepsilon_2)^2 + (\varepsilon_3)^2\}}$$

where, ε_i, represents the principal strains ($\varepsilon_1 > \varepsilon_2 > \varepsilon_3$). In the calculation of the von-Mises equivalent strain, $\varepsilon_1 + \varepsilon_2 + \varepsilon_3 = 0$ was assumed, as the strain is primarily plastic strain and

satisfies the constant volume condition, with a small amount of elastic strain.

The surface of the tensile specimen was painted with black and white inks to produce speckle patterns (random dot patterns), serving as markers for tracking each identical position of specimens during DIC strain analysis. A CCD camera (SVS625MFCP, SVS-VISTEK) continuously captured images of the patterned surface at a constant rate of 5 fps (frame per second) until fracture. The captured images were analyzed using DIC-dedicated software (Vic-2D, Correlated solutions). In DIC analysis, the subset size and step size (interval of inspecting point) were set to 106.95 μm and 17.25 μm, respectively.

For microscopic-DIC (μ-DIC) analysis in the SEM, mini-sized dog-bone-shaped tensile specimens with a gauge length of 5 mm, a gauge width of 2.5 mm and a thickness of 1 mm were used. The specimen geometry is shown in **Fig. S1**(b) in the supplementary materials. Prior to tensile testing, the surface of each mini-sized tensile specimen was electro-polished, and a grid pattern was introduced using a focused ion beam (FIB; FEI Quanta 3D 200i), aiming to provide additional strong contrast with microstructure-originated contrast. The FIB-grid lines improve the reliability of DIC strain analysis by preventing the formation of unexpected slip lines, which primarily occur in ferrite grains and can reduce the precision of the analysis. The tensile test was interrupted at specific strain levels, and the same area was observed in the SEM under each tensile strain condition. The subset size and step size were set to 2.953 μm and 0.328 μm, respectively, for μ-DIC analysis.

2.4. Nano-hardness of each phase

A nano-indentation test was conducted to evaluate the hardness of ferrite and martensite in the isolated DP and chained DP specimens using a Berkovich-typed tip under a maximum load of 350 μN with a holding time of 0.5 seconds, using a nano-indentation testing machine (TI 950 TriboIndenter, Hysitron). For each specimen, 465 data points were acquired to ensure statistical reliability in the hardness measurements of the constituent phases.

3. Results

3.1. Microstructure observations and nano-hardness

Fig. 3(a) and (b) show SEM micrographs of DP structures obtained through (a) Route 1 and (b) Route 2 heat treatments as shown in **Fig. 2**. In SEM contrast, the ferrite (F) appears darker, while the martensite (M) appears brighter. Two SEM images (a) and (b) exhibited

isolated DP and chained DP structures, respectively. The average ferrite grain sizes for isolated DP and chained DP structures were measured to be 3.9 μm and 3.2 μm, respectively, with martensite volume fractions of 34% and 30%, respectively. **Fig. 3**(c) and (d) demonstrate the nano-hardness distribution of ferrite and martensite in (c) isolated DP and (d) chained DP structures. The average hardness value of ferrite in isolated DP and chained DP structures was 2.9 ± 0.46 GPa and 2.8 ± 0.32 GPa, respectively. The average hardness of martensite in the isolated DP and chained DP structures was 6.7 ± 1.71 GPa and 6.2 ± 1.70 GPa, respectively. The martensite exhibited a wide distribution in hardness, which might be attributed to its complicated substructure, including different crystallographic orientations and heterogeneity in dislocation distribution [29-32]. The obtained nano-hardness results indicate that martensite shows more than twice the hardness value compared to ferrite in both DP specimens. No significant difference in the phase hardness (i.e., hardness for ferrite or martensite) was observed between both DP specimens, while the martensite showed a slight difference in hardness average. The microstructure characterization revealed that both DP structures showed a significant difference only in martensite distribution, while their ferrite grain size, phase fraction and phase strength (hardness) remained similar.

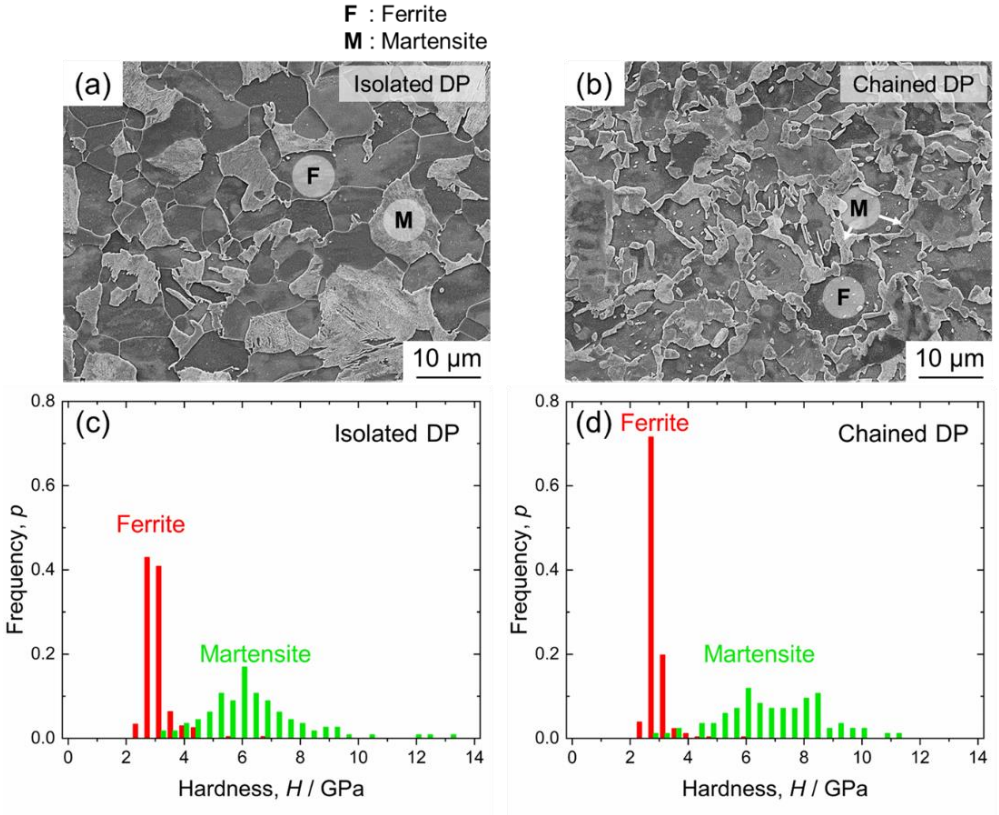


Fig. 3 (a, b) SEM micrographs of DP structures having (a) isolated martensite distribution and (b) chained martensite distribution, obtained from the heat treatments of Route 1 and Route 2 in Fig. 2, respectively. (c, d) Nano-hardness distribution of ferrite and martensite phases for (c) the isolated DP and (d) the chained DP specimens.

3.2. Tensile properties

Fig. 4(a) exhibits engineering stress-strain (S-S) curves for the isolated DP (blue line) and chained DP (red line) structures. Uniform elongation is indicated by an open square symbol on each stress-strain curve. The yield strength (σ_{YS}: 0.2% proof stress), tensile strength (σ_{TS}), uniform elongation (e_U) and total elongation (e_T) obtained from stress-strain curves were summarized in **Table 1**. The chained DP specimen showed slightly higher tensile strength than the isolated DP specimen. In terms of ductility, the chained DP specimen demonstrated a significantly larger uniform elongation of 0.132 and a total elongation of 0.253, compared to the isolated DP specimen with a uniform elongation of 0.107 and a total elongation of 0.198. Uniform elongation can be understood in terms of strain-hardening behavior according to the Considère criterion [33], where macroscopic necking occurs when the strain-hardening rate becomes smaller than the value of true stress. **Fig. 4**(b) displays true stress-true strain curves for the isolated DP (blue) and chained DP (red) specimens, together with strain-hardening rate

curves. The crossing point of the strain-hardening rate curve and the true stress-strain curve is marked by an open square symbol. Both specimens showed a typical strain-hardening rate curve that decreased monotonously with plastic deformation. However, the chained DP specimen maintained a slightly larger strain-hardening rate value throughout the entire range of tensile deformation. As a result, the strain-hardening rate curve in the chained DP specimen intersected its true stress-strain curve at the higher strain value. This indicates that the large uniform elongation observed in the chained DP specimen might be attributed to its enhanced strain-hardening ability. In addition, **Fig. 4**(c) shows n-value ($(d(\ln\sigma)/d(\ln\varepsilon))$) as a function of true strain, ε. The curve intersects with n=ε, indicating the onset of plastic instability. It was found that the onset of plastic instability identified by the n-value analysis closely corresponded with the results obtained from the strain-hardening rate analysis. To further investigate overall ductility, including post-uniform elongation accompanied by necking development, a DIC-strain analysis was conducted.

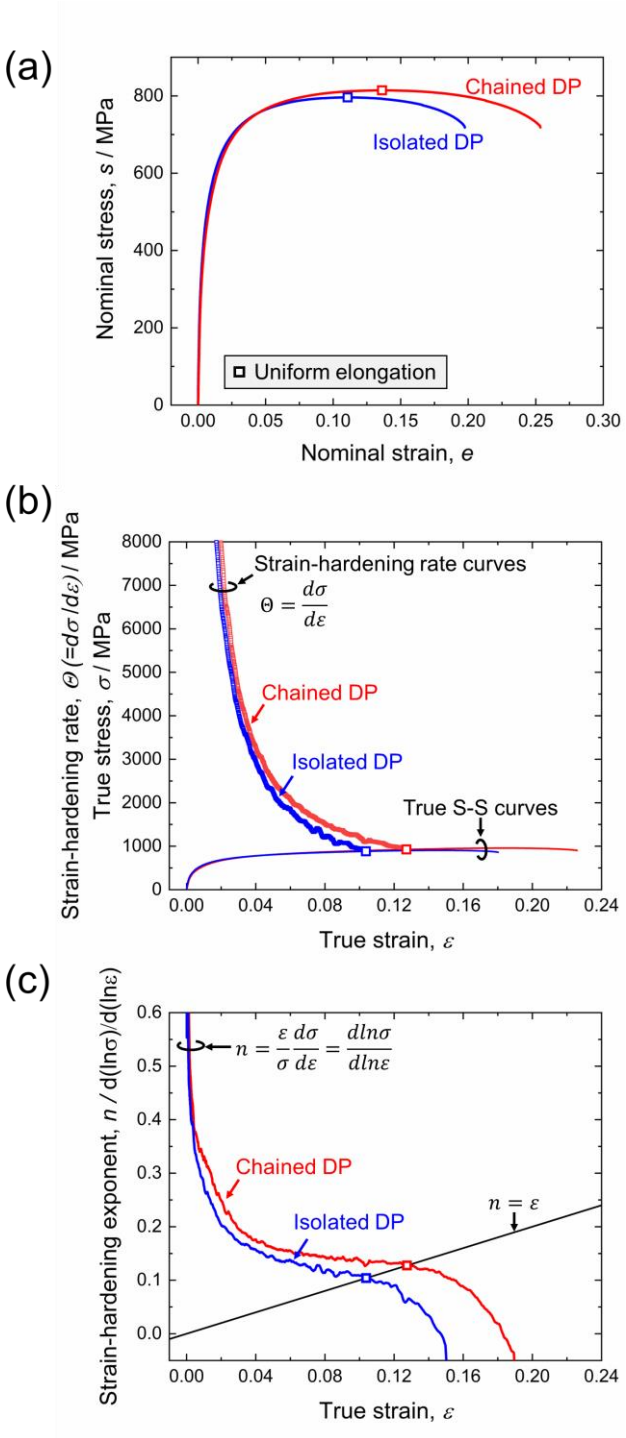


Fig. 4 (a) Engineering stress-strain (S-S) curves of the isolated DP and the chained DP specimens. A square symbol on each S-S curve indicates uniform elongation. (b) Strain-hardening rate curves and true S-S curves of the isolated DP and the chained DP specimens. Each square symbol indicates the crossing point of the strain hardening rate curve and true S-S curve. (c) n-value (d(ln σ)/d(ln ε)) as a function of true strain, ε. The curve intersects with n=ε, indicating the onset of plastic instability.

Table 1 Summary of tensile property details of the isolated DP and chained DP specimens.

Specimen	Yield strength, σ_{YS} / MPa	Tensile strength, σ_{TS} / MPa	Uniform elongation, e_U	Total elongation, e_T
Isolated DP	420	796	0.107	0.198
Chained DP	376	807	0.132	0.253

3.3. Local deformation behavior at specimen scale

Fig. 5 displays DIC-strain distribution maps of tensile specimens with (a) isolated DP structure and (b) chained DP structure at the specific tensile strains of 6%, 12%, 18% and 24%. The tensile direction is parallel to the horizontal direction (defined as the x-direction) of images, and the colors superimposed on the specimens correspond to a key strain color bar representing the normal strain component in the tensile direction (ε_{xx}). At a tensile strain condition of 6%, both specimens exhibited nearly homogeneous deformation throughout the gauge part. At 12% tensile strain, slight strain localization was observed in the gauge part of the isolated DP specimen, whereas the chained DP specimen maintained homogeneous deformation. When the tensile strain reached 18%, the isolated DP specimen showed a strong strain localization, with the center part experiencing a high local strain value of 0.63. In contrast, the chained DP specimen at 18% tensile strain did not exhibit apparent strain localization in the gauge part, with a maximum local strain of 0.21. The isolated DP specimen fractured at the tensile strain of 19.8%. At a tensile strain of 24% for the chained DP specimen, a strong strain localization with a maximum strain value of 0.68 was observed. This strongly suggests that the chained DP structure inhibits rapid strain localization and has an outstanding strain capacity that can endure extremely large strain (ε_{xx}^{max}= 0.68) in the necked region. The higher strain-hardening ability of the chained DP specimen is believed to suppress necking evolution by further hardening the necking region, allowing deformation to propagate to neighboring areas and alleviating strain localization of the necking-initiated region. Such distinct local deformation behaviors observed in the two DP tensile specimens may arise from their characteristic microstructural features, particularly the different distributions of martensite.

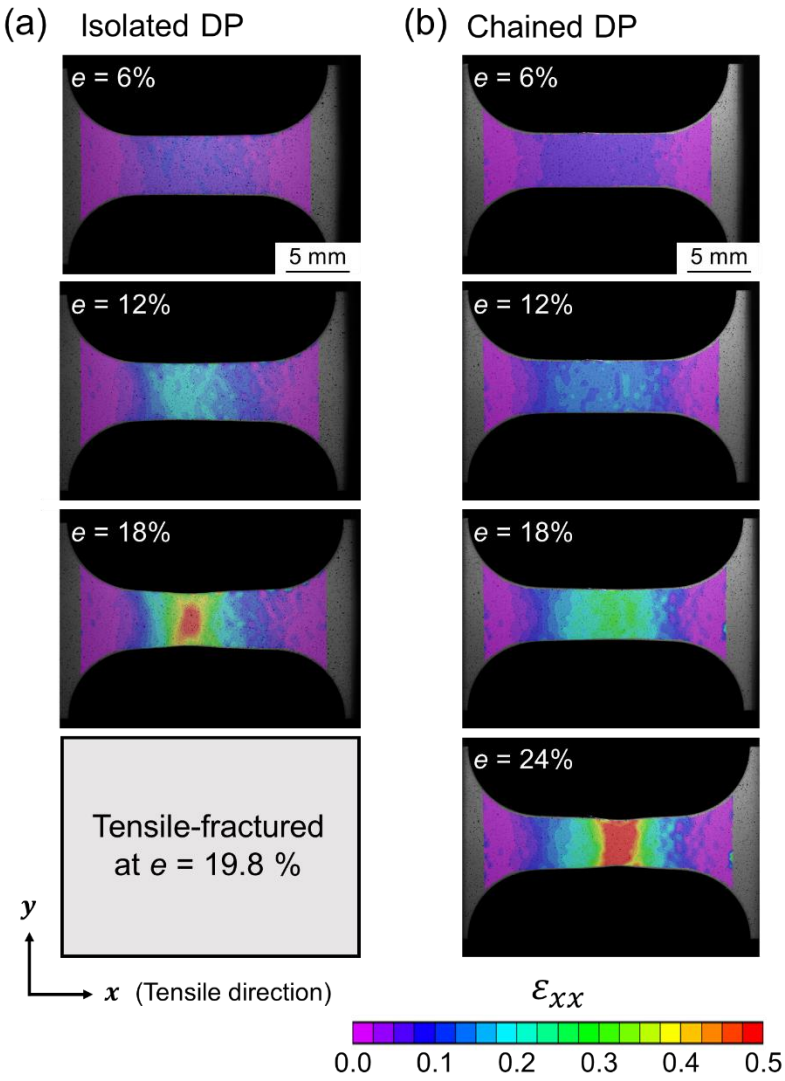


Fig. 5 DIC-strain distribution maps of tensile specimens of (a) the isolated DP structure and (b) the chained DP structure at the specific tensile strain of e = 6%, 12%, 18% and 24%. The tensile direction is parallel to the horizontal axis of the images, and the colors superimposed on the tensile specimens indicate the value of the normal strain component (ε_{xx}) in the tensile direction, according to the key strain color bar.

3.4. Local deformation behavior in microstructures

Fig. 6 shows DIC-strain distributions of the (a) isolated DP specimen and the (b) chained DP specimen at a global tensile strain of 1.8%. The tensile direction is parallel to the horizontal direction (defined as the x-direction) of images, and colors on the maps indicate the value of a normal strain component (ε_{xx}) in the tensile direction. Ferrite/martensite boundaries were indicated by white lines in the top row strain maps, and extracted DIC-strain maps for ferrite and martensite were shown in the middle and bottom rows, respectively.

It is noteworthy that both DP specimens exhibit very different strain distributions. In the isolated DP specimen, significant strain localization occurred in the ferrite regions, particularly near martensite with large size, and it tended to be distributed along ferrite/martensite boundaries. The martensite in the isolated DP specimen did not mostly contribute to deformation, except in very local regions near the ferrite/martensite boundaries. In contrast, the chained DP specimen exhibited more homogeneous deformation. Strain localization in the ferrite was weaker, and a significant portion of martensite contributed to the deformation (see bottom row of **Fig. 6** (b)).

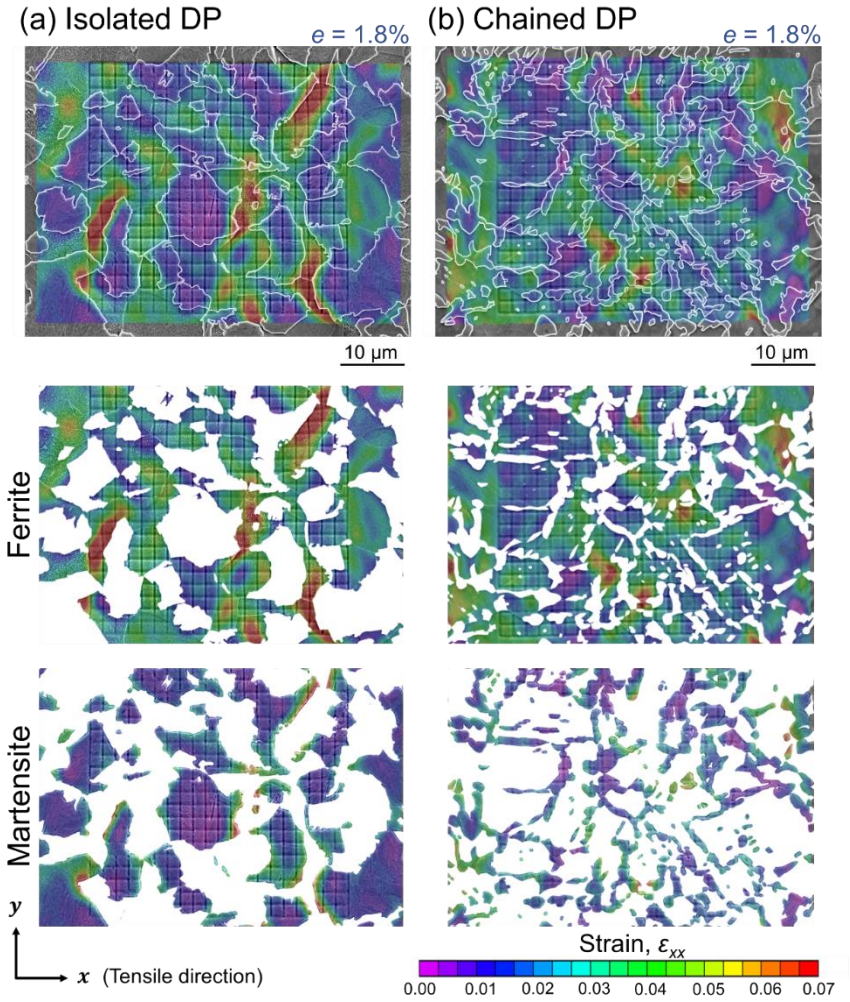


Fig. 6 μ-DIC local strain distribution maps of (a) isolated DP specimen (b) chained DP specimen at the tensile strain of 1.8%. The tensile direction is along the horizontal axis of the images, and the colors indicate the normal strain component (ε_{xx}) in the tensile direction. Ferrite/martensite boundaries are marked by white solid lines on the strain maps in the top row. Selectively extracted strain maps for the ferrite region and the martensite region are shown in the middle and bottom rows, respectively.

In addition, the strain distribution maps for ε_{xx}, ε_{yy}, and ε_{xy}, along with the von-Mises equivalent strain (ε_{eq}) map, are presented in **Fig. 7**. It was observed that the ε_{yy} map exhibits an opposite trend to the ε_{xx} map, while the shear strain map, ε_{xy}, exhibits significant changes primarily at the boundaries. Interestingly, the von-Mises equivalent strain map (ε_{eq}) shows a distribution very similar to that of the ε_{xx} map. This suggests that the local strain conditions roughly follow the uniaxial tensile condition (i.e., $\varepsilon_{xx} \approx \varepsilon_{eq}$ under ideal tensile deformation).

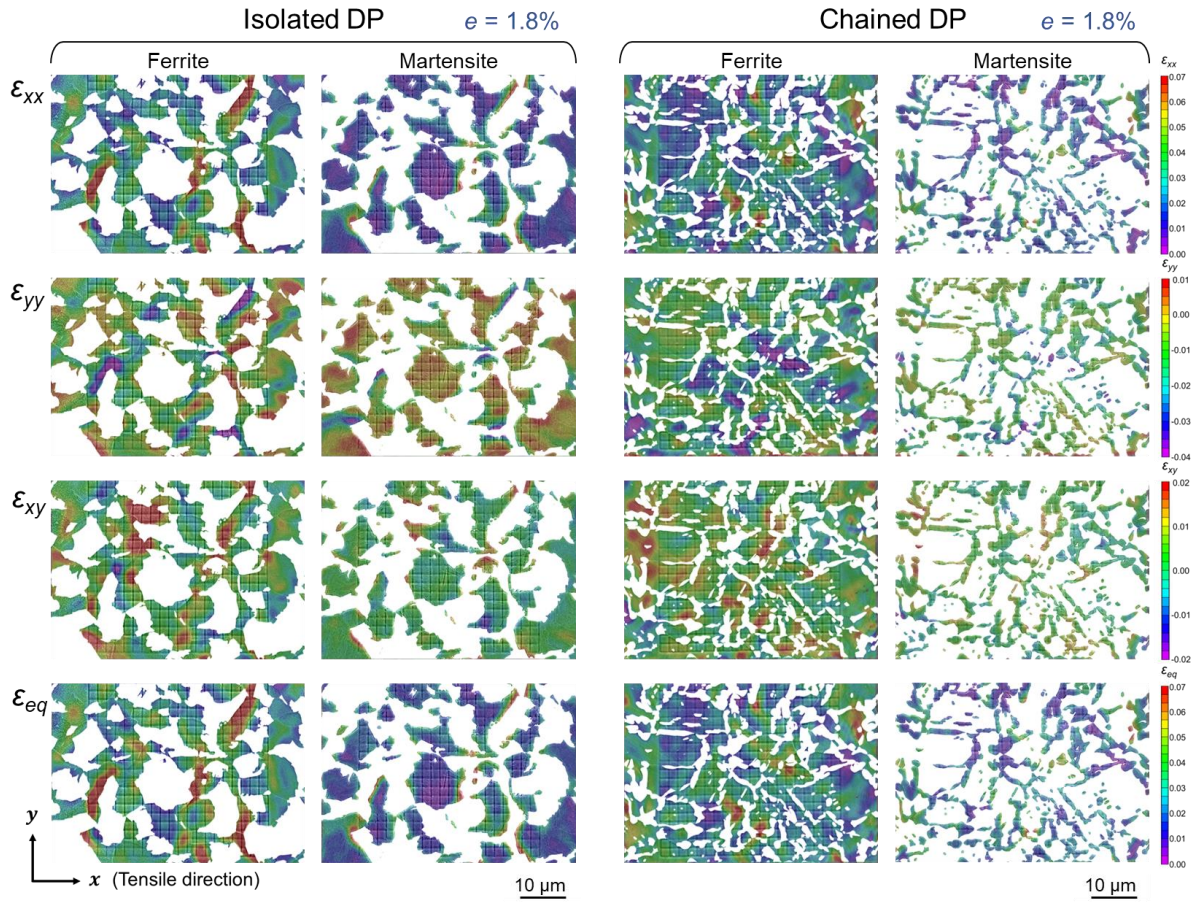


Fig. 7 ε_{xx}, ε_{yy}, ε_{xy}, and ε_{eq} local strain distribution maps of (a) isolated DP specimen (b) chained DP specimen at the tensile strain of 1.8%.

Fig. 8 shows the evolution of strain distributions in (a) isolated and (b) chained DP specimens with further deformation at a global tensile strain (e) of ~5% (top row), ~10% (medium row) and ~18% (bottom row). In the strain maps, **F** and **M** denote ferrite and martensite, respectively. Strain values (ε_{xx}) in each strain map can refer to the corresponding key strain color bar on the same row. Yellow arrows in the strain maps for the isolated DP specimen indicate representative micro-cracks with large sizes. Although the absolute value of local strain increases with tensile deformation, it is interesting to note that the overall trend

of strain distributions seems maintained even to a heavily deformed state (e~18%). In the isolated DP specimen, extremely strong strain localization was found in ferrite, near which several large-sized micro-voids were observed. More interestingly, the large-sized martensite in the isolated DP specimen did not deform even at e = 18.2%. In the chained DP specimen, in contrast, no strong strain localization and no large-sized micro-voids were observed, maintaining homogeneous deformation.

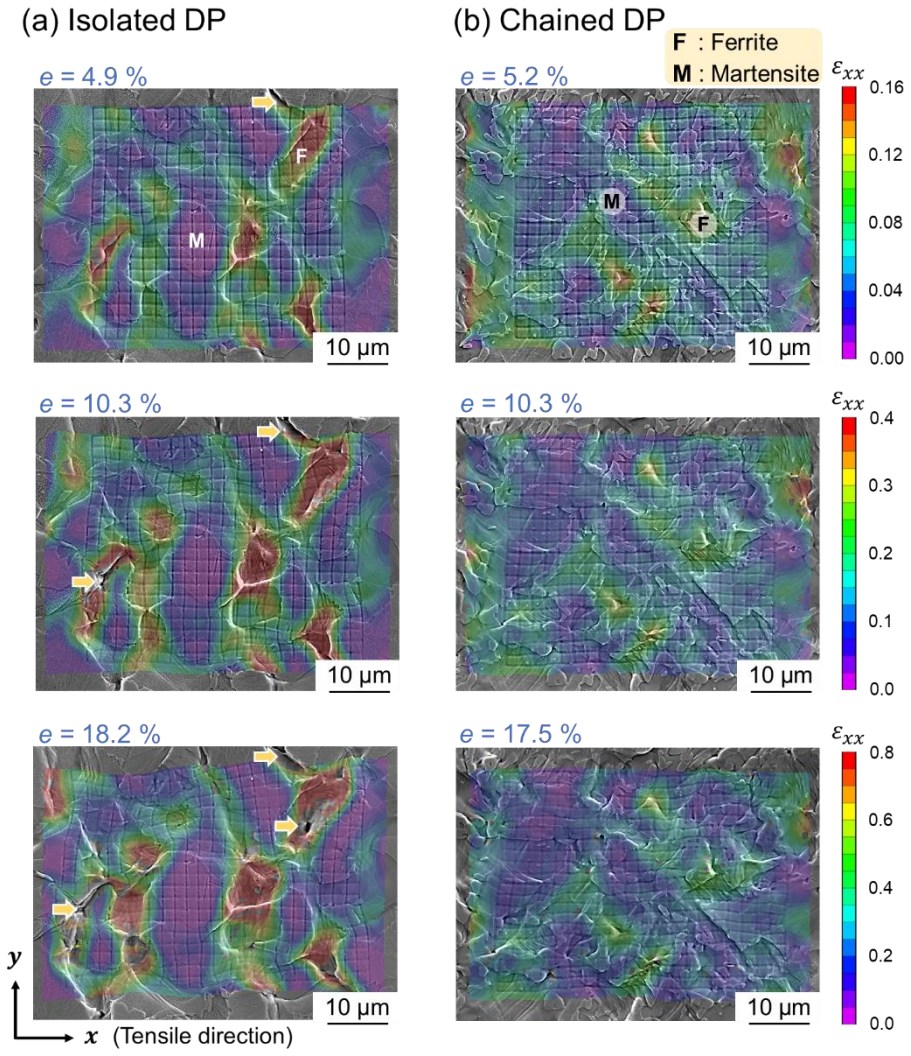


Fig. 8 Evolution of local strain distribution of (a) the isolated DP specimen at the tensile strain of e = 4.9%, 10.3% and 18.2% and (b) the chained DP specimen at the tensile strain of e = 5.2%, 10.3% and 17.5%. Yellow arrows indicate micro-voids with significantly large sizes. Strain values (ε_{xx}) in each strain map correspond to the key strain color bar on the same row.

Fig. 9 shows the frequency histograms of strain components (ε_{xx}, ε_{yy}, and ε_{xy}) and the von-Mises equivalent strain (ε_{eq}) for ferrite and martensite phases in (a) the isolated DP specimen

tensile-deformed to 18.2% and in (b) the chained DP specimen tensile-deformed to 17.5%. The strain histograms for the two DP specimens exhibit notable differences. In the ε_{xx} strain histogram, the isolated DP specimen showed an apparent separation of histograms for ferrite and martensite, among which martensite particularly exhibited a right-skewed distribution due to a large portion of undeformed martensite. Many martensite regions remain undeformed, while some ferrite regions experience extremely high strains exceeding 0.6. In contrast, the chained DP structure exhibited mostly overlapping histograms, indicating that martensite contributed significantly to deformation, and that nearly all the ferrite regions avoid extremely high strains. The ε_{yy} strain histogram reveals an opposite trend to ε_{xx}, with the isolated DP specimen showing markedly heterogeneous deformation. ε_{xy} shear strain histogram displays considerable variability, particularly in the ferrite phase. The ε_{eq} histogram is similar to the ε_{xx} strain histogram, suggesting that the local strains approximate a uniaxial tensile deformation condition.

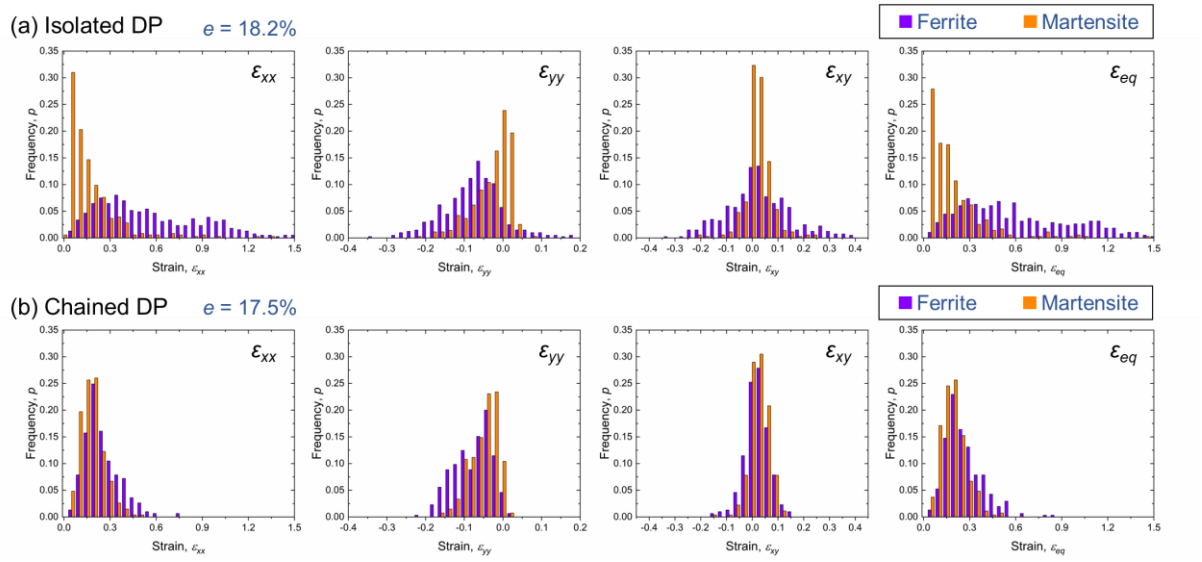


Fig. 9 Frequency histograms of strain components (ε_{xx}, ε_{yy}, and ε_{xy}) and the von-Mises equivalent strain (ε_{eq}) for ferrite (purple) and martensite (orange) phases in (a) the isolated DP specimen tensile-deformed to 18.2% and in (b) the chained DP specimen tensile-deformed to 17.5%.

4. Discussion

4.1. Boundary characterization

We found that the chained DP specimen exhibited better ductility than the isolated DP structure. This improvement could be attributed to the significant suppression of strain localization in ferrite grains, with a greater contribution of martensite to plastic deformation. Such a significant difference in deformation heterogeneity might be related to the spatial configuration of the boundary and its density. It is believed that the ferrite/martensite boundary, confining displacements of ferrite and martensite, would be the predominant site where strain-partitioning occurs. **Fig. 10**(a) and (b) display SEM microstructures and corresponding ferrite/martensite (F/M) + ferrite/ferrite (F/F) boundary maps in the (a) isolated DP and (b) chained DP specimens. **Fig. 10**(c) shows a quantitative result of boundary density. The F/M and F/F boundaries were expressed in red and blue colors, respectively. Significant differences in boundary density and boundary fractions were observed between the two DP specimens. Line fraction of F/M boundary and F/F boundary for the isolated DP specimen accounted for 72% (0.37 μm^{-1}) and 28% (0.14 μm^{-1}), respectively, but the chained DP structure was mostly composed of F/M boundary (95% (0.77 μm^{-1})) with a very small portion of F/F boundaries (5% (0.04 μm^{-1})). The chained DP specimen had a significantly higher boundary density of 0.81 μm^{-1} in total, compared to the isolated DP specimen (0.51 μm^{-1} in total). The F/M boundary is considered the primary factor promoting martensite deformation, which may explain our experimental result showing homogeneous deformation in the chained DP specimen with a high F/M boundary density.

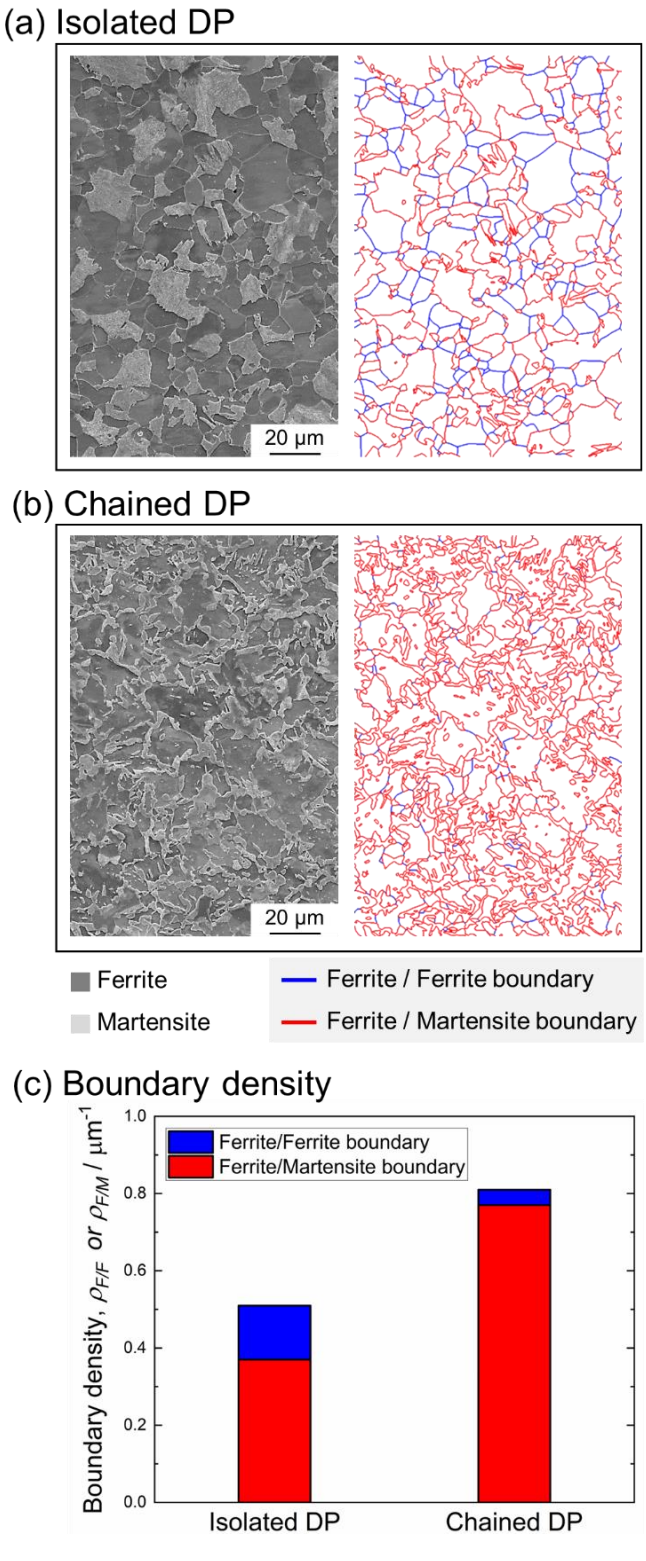


Fig. 10 (a, b) SEM micrographs and corresponding boundary maps of ferrite/martensite boundary (red) and ferrite/ferrite boundary (blue) in (a) isolated DP specimen and (b) chained DP specimen. (c) Quantitative result of boundary densities (μm^{-1}) of ferrite/martensite (red) and ferrite/ferrite boundaries (blue) in isolated and chained DP specimens.

4.2 Dependence of deformation behavior on martensite size

From the DIC-strain distribution results shown in **Fig. 6** and **Fig. 8**, it can be noticed that the large-sized martensite in the isolated DP specimen deformed only in the vicinity of the ferrite/martensite (F/M) boundary, but the center region of martensite hardly contributed to deformation even at heavily deformed states. This indicates that the distance from the F/M boundary in martensite may also be a significant factor influencing deformation behavior, and possibly there is a critical deformation-affectable distance. **Fig. 11** exhibits strain profiles (ε_{xx} and ε_{yy}) for (a) isolated DP and (b) chained DP specimens at different tensile strains. The lines for the strain profile were indicated on each DIC-strain map. Vertical solid lines on the graphs indicate F/M boundaries. In the martensite of the isolated DP specimen, a non-plastically deformed zone was observed in the center part having a width of 8.2 μm, but only the regions having a width of 1.9 μm (left side) and 2.7 μm (right side) from F/M boundaries deformed. Namely, 64% of the martensite did not contribute to deformation (ε_{xx} and ε_{yy}) even at the heavy deformation state (e = 14.8%). Such an uncooperative deformation contribution of martensite eventually leads to strong strain localization in the ferrite and even in the martensite itself near F/M boundaries. The ferrite endured extremely high strain reaching ε_{xx} = 0.7, and the deformed martensite regions near F/M boundaries also managed a quite high strain reaching ε_{xx} = 0.5~0.6, which is an extremely high strain value for martensite. In contrast, in the chained DP specimen, the non-plastically deformed zone was not found. Three martensite particles, having a thickness of 3.8 μm, 3.3 μm and 0.9 μm, were inspected, and all of them exhibited a gradual increase in strains (see the arrows indicating the strain changes in the green-colored regions in **Fig. 11** (b)). Considering that one martensite particle has two F/M boundaries on both sides, it would be reasonable to infer that the thickness scale ranging 3~4 μm is in the deformation-affectable regions. In terms of minimizing strain localization to achieve large ductility, the size of martensite should be controlled to smaller sizes to avoid the formation of a non-plastically deformed zone. Although the current analysis only shows one example of highly localized regions, such trends can be easily observed elsewhere in **Fig. 8**. Still, however, the scientific origin of the occurrence of the non-plastically deformed zone and deformation-affectable distance is still unclear, which will be assessed in future work. In addition to martensite size, other microstructural factors—such as the misorientation between ferrite and martensite at the F/M boundaries, spatial inhomogeneity in martensite fraction, and martensite connectivity (degree of chain formation)—should be considered to deepen our understanding of the deformation behavior of DP structures, which will also be explored in

future studies. Furthermore, the present study concludes that the limited ductility in the isolated DP specimen is primarily due to the heterogeneous deformation, with martensite contributing less to plastic deformation. However, spatial inhomogeneity in the martensite fraction (i.e., the presence of local areas with high martensite fraction due to several large-sized martensite regions) could also be a contributing factor to the reduced ductility. A further quantitative evaluation of spatial inhomogeneity in martensite fraction is necessary.

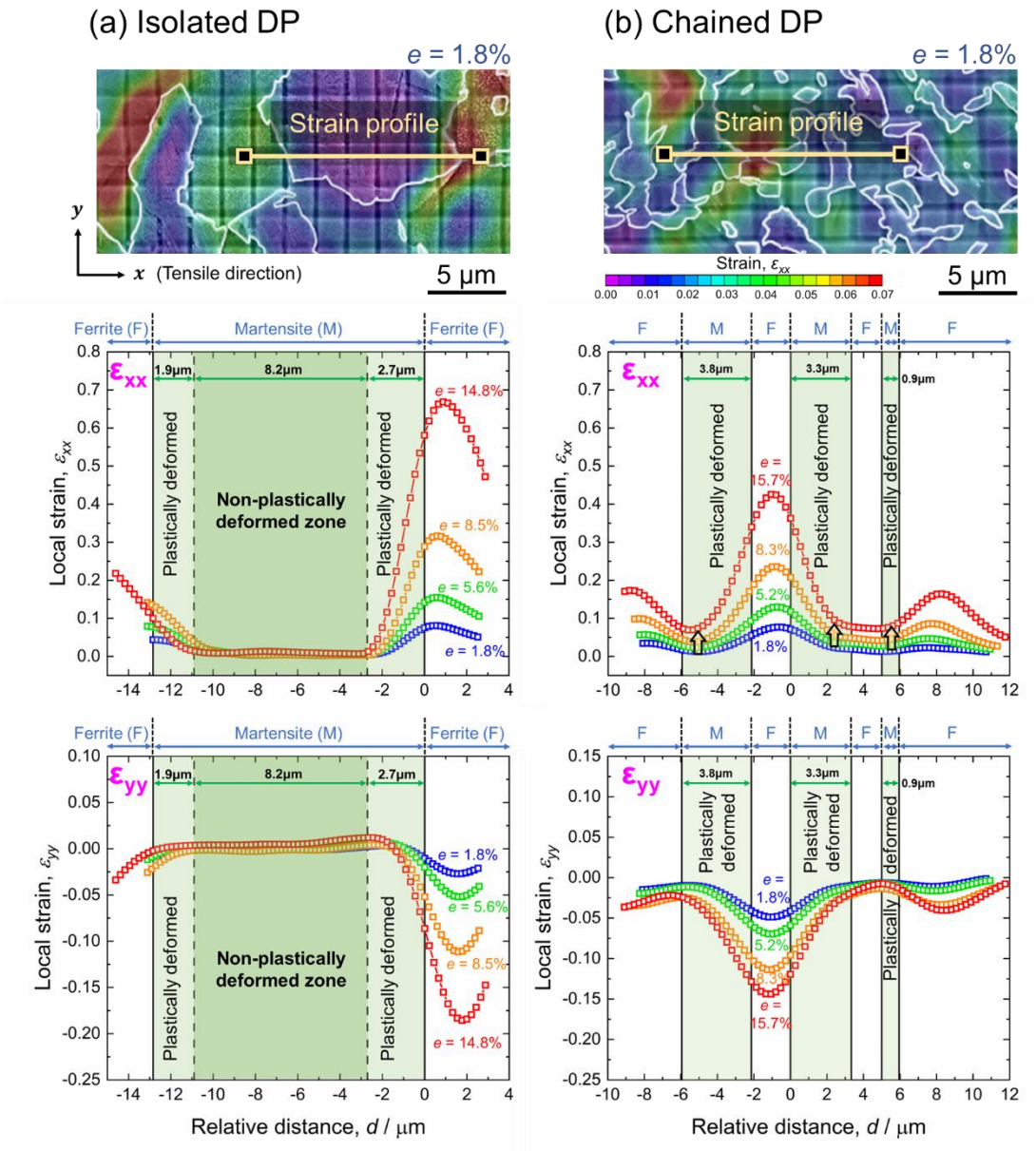


Fig. 11 Strain profiles (ε_{xx} and ε_{yy}) for (a) isolated DP and (b) chained DP specimens at different tensile strains (e = 1.8%, 5.6%, 8.5% and 14.8% for isolated DP, and e = 1.8%, 5.2%, 8.3% and 15.7% for chained DP). Lines for the strain profile were indicated on each DIC-strain map, and vertical solid lines in the graphs mark the position of F/M boundaries. The dashed lines

in the graphs of the isolated DP specimen denote the boundary between "plastically deformed" and "non-plastically deformed" zones.

4.3 Micro-void evolution during deformation

It has been reported that micro-void formation and its evolution in DP structures play a critical role in mechanical properties, especially ductility [10, 26]. In this section, the micro-void number and their spatial distribution were characterized and discussed in association with local deformation behavior. **Fig. 12**(a) shows the number of micro-voids as a function of distance from the fracture surface of the tensile-fractured specimen. A schematic sketch was inserted in the graph for reference. In both DP specimens, the number of micro-voids peaked near the fracture surface and drastically decreased with increasing distance from the fracture surface. However, the absolute number of micro-voids between both DP specimens differed substantially, especially near the fracture surface. At a distance of 100 μm from the fracture surface, the chained DP specimen had four times more micro-voids (n_{void} = 138) than the isolated DP specimen (n_{void} = 31). It is interesting to note that despite having a higher number of micro-voids, the chained DP exhibited greater ductility, suggesting that additional factors should be considered in understanding its enhanced ductility. **Fig. 12**(b) and (c) exhibit micro-void distributions and their number-frequency of the tensile-fractured (b) isolated DP and (c) chained DP specimens, both observed at a distance of 100 μm from the fracture surface. Enlarged images were provided, in which all micro-voids identified through careful SEM observation were indicated by arrows. In the isolated DP microstructure (**Fig. 12**(b)), relatively a large portion of large-sized micro-voids (> 2μm) were observed (6 voids among 31 voids), and some micro-voids, marked by red arrow, were aligned at a tilting angle of 65° to the tensile direction. The region with linearly aligned micro-voids likely experienced greater deformation, resulting in a more indented surface compared to the surrounding areas, suggesting that the linear alignment of voids is a consequence of localized deformation. Indeed, although the void-investigated area is not the exact site where the fracture actually occurs, it is believed to be one potential site that can lead to fracture through the coalescing process of aligned micro-voids. In contrast, in the chained DP structure (**Fig. 12**(c)), a large number of micro-voids were observed, most of which remained small, existing in the size range of 0.5 μm to 2.0 μm without specific alignments in distributions. Large-sized micro-voids (> 2μm) were also observed in the chained DP specimen, but the fraction of them was likely small, with only 9 voids observed among 138 voids. The results of micro-void distributions suggest that the spatial distribution/alignment of large-sized micro-voids can be one critical factor in

regulating the fracture behavior of DP structures. Kadkhodapour et al. [26] claimed that the micro-voids were arranged predominantly on the shear band (deformation band) based on their experiment and FEM (finite element method) simulation results, which implied that the micro-void distribution is closely related to the local deformation distributions.

Considering the local strain value of the necked region (see **Fig. 5**), the chained DP specimen underwent a larger strain localization (ε_{xx}^{max}=0.68) than the isolated DP specimen (ε_{xx}^{max}=0.63). However, in the microstructure, no significant void growth was found in the chained DP specimen even at such an extremely strain-localized condition, which would be related to its characteristic local strain distribution exhibiting relatively homogeneous deformation. **Fig. 12**(d) and (e) are representative examples showing micro-void evolution during deformation with investigation of local strain distribution in (d) isolated DP and (e) chained DP specimens. The position at which the micro-void occurs was indicated by arrows on SEM microstructures. In the isolated DP structure, the observed micro-void was formed along the highly strain-partitioned F/M boundary at a relatively large tensile strain level (e = 12.6% to 19.1%). The micro-void growth progresses along the F/M boundary, and such situations will primarily happen on the strain-localized band. In the chained DP structure, the micro-void was observed at the neck-shaped martensite segment at the relatively early tensile strain of 8.9%, with a quite small local strain value lower than 0.06, around which no significant strain localization occurred. The void growth occurred at the later stage of deformation (e = 18.8%), but the size only reached approximately 1 μm. This is probably due to sufficient plasticity of ferrite embedding the micro-void, and such situations can eventually suppress void growth effectively.

The present study is believed to suggest the importance of microstructure control in DP structures for enhancing tensile properties, especially in ductility, which can be understood in terms of the following achievements: (i) Increasing ferrite/martensite boundary fraction, (ii) maintaining a small size of martensite and (iii) suppressing strain localization in ferrite. We believe that the effect of grain refinement in DP structures, reported to exhibit good mechanical properties [1, 2, 7], would also be related to these achievements—at least, (i) and (ii) are satisfied by grain refinement of ferrite and martensite. In the next study, the effect of all the microstructure factors, including grain size, phase hardness and phase fraction, will be investigated by estimating the degree of three achievements. Finally, a universal strategy for the optimal microstructure control to further enhance mechanical properties will be proposed.

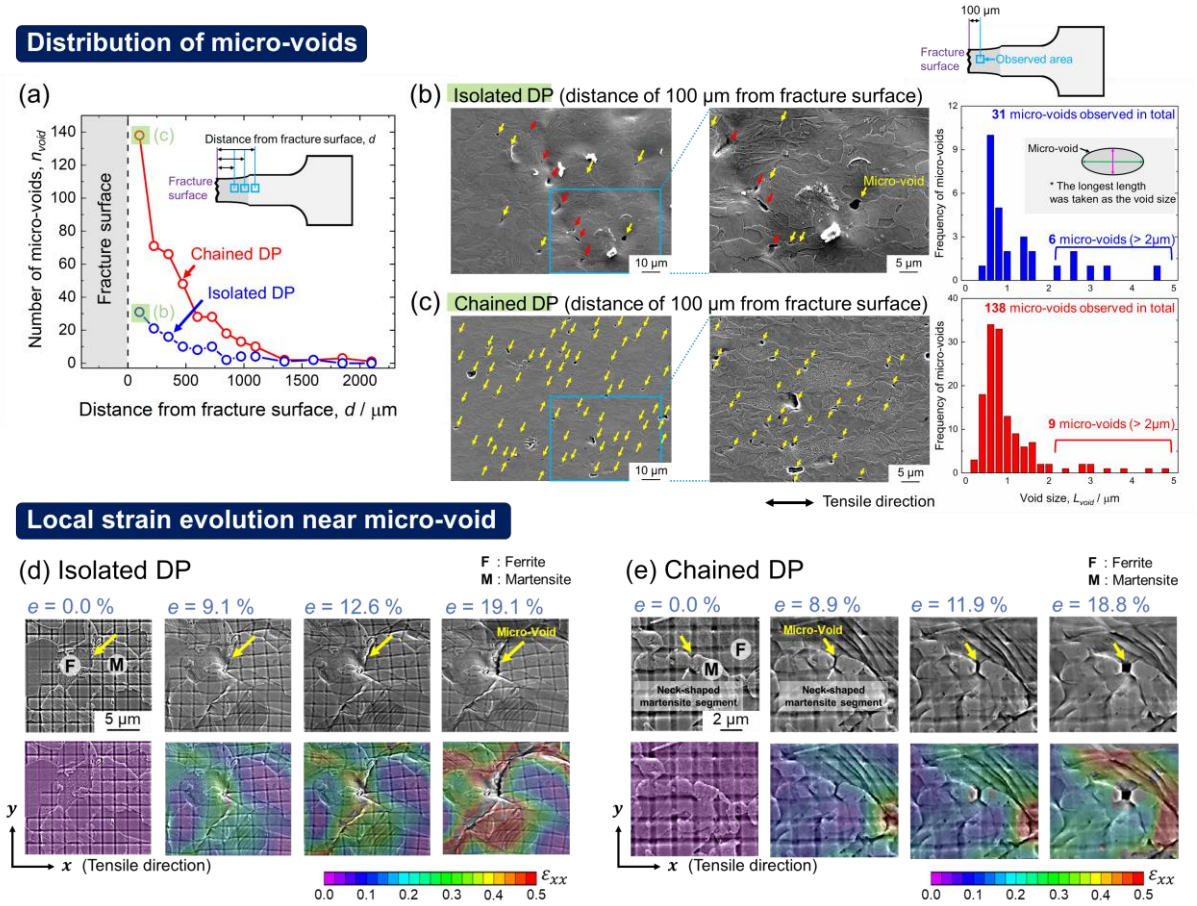


Fig. 12 (a) The number of micro-voids as a function of distance from the fracture surface of the tensile-fractured specimen. A schematic sketch was inserted in the graph for reference. (b, c) Micro-void distributions and their number-frequency of tensile fractured (b) isolated and (c) chained DP specimens, observed at a distance of 100 μm from the fracture surface. Micro-voids are marked by arrows, among which arrows in red indicate relatively large-sized micro-voids with linear alignment. (d, e) Examples showing micro-void evolution during deformation with investigation of local strain distribution in (d) isolated DP and (e) chained DP specimens.

5. Conclusions

In the present study, the mechanical property and local deformation behavior of ferrite + martensite dual phase (DP) steel having different martensite distributions were systematically characterized by using digital image correlation (DIC) analysis and careful identical area observation in tensile deformation. The main conclusions obtained are as follows:

(1) Two types of DP structures having an isolated martensite distribution (isolated DP) and a chained martensite distribution (chained DP) were successfully fabricated by different heat treatment schedules. Except for martensite distributions, other several microstructure factors, such as ferrite grain size, martensite fraction and phase hardness, were almost identical in both two DP specimens.

(2) The chained DP specimen exhibited significantly large ductility (0.253 in total elongation), with a slight increase in strength (807 MPa in ultimate tensile strength (UTS)) compared to the isolated DP specimen (0.198 in total elongation and 796 MPa in UTS). The chained DP specimen showed a higher strain-hardening ability than the isolated DP specimen, which was believed to be the reason for the enhanced uniform elongation of the chained DP specimen.

(3) The μ-DIC strain analysis exhibited very different local strain behavior depending on the martensite distributions: The chained DP specimen exhibited relatively homogeneous deformation with more deformed martensite whereas the isolated DP specimen showed strong strain localization in ferrite grains due to less deformed martensite. It is believed that more homogeneous deformation achieved in the chained DP specimen leads to a significant enhancement of tensile elongation.

(4) A great number of micro-voids were observed in the chained DP specimen, and they were distributed in a nearly random manner. In contrast, the isolated DP specimen had fewer amounts of micro-voids, but some of them were laid keeping a specific arrangement with an inclination angle of 65 degrees to the tensile axis. This suggests that the distinct micro-void distributions result from markedly different strain distribution characteristics between the chained DP and isolated DP specimens.

Acknowledgment

This research work was financially supported by the Elements Strategy Initiative for Structural Materials (ESISM; JPMXP0112101000), JST CREST (JPMJCR1994), and KAKENHI (Grant-in-Aid for Scientific Research from the Japan Society for the Promotion of Science; JP22K18888, JP23H00234, JP23K20037, JP20K14608 and JP24K07214), all from the Ministry of Education, Culture, Sports, Science and Technology (MEXT), Japan. All the supports are gratefully appreciated.

Conflict of interest

The authors declare no conflicts of interest.

Author contributions

M-H.P. was responsible for this research. M-H.P. and R.M. carried out most of experiments and analysis. A.S. carried out nano-indentation test and characterized micro-void evolution. M-H.P. and N.T. wrote the paper. All authors discussed the results, and checked and revised the manuscript.

References

[1] M. Delincé, Y. Bréchet, J.D. Embury, M.G.D. Geers, P.J. Jacques, T. Pardoen, Structure-property optimization of ultrafine-grained dual-phase steels using a microstructure-based strain hardening model, *Acta Mater*. **55** (2007) 2337–2350. https://doi.org/10.1016/j.actamat.2006.11.029.

[2] M.H. Park, A. Shibata, N. Tsuji, Effect of Grain Size on Mechanical Properties of Dual Phase Steels Composed of Ferrite and Martensite, *MRS Adv*. **1** (2016) 811–816. https://doi.org/10.1557/adv.2016.230.

[3] M. Mazinani, W.J. Poole, Effect of martensite plasticity on the deformation behavior of a low-carbon dual-phase steel, *Metall. Mater. Trans. A Phys. Metall. Mater. Sci.* **38** (2007) 328–339. https://doi.org/10.1007/s11661-006-9023-3.

[4] A. Ebrahimian, S.S. Ghasemi Banadkouki, Mutual mechanical effects of ferrite and martensite in a low alloy ferrite-martensite dual phase steel, *J. Alloys Compd*. **708** (2017) 43–54. https://doi.org/10.1016/j.jallcom.2017.02.287.

[5] J. Samei, D.E. Green, J. Cheng, M.S. de Carvalho Lima, Influence of strain path on nucleation and growth of voids in dual phase steel sheets, *Mater. Des*. **92** (2016) 1028–1037. https://doi.org/10.1016/j.matdes.2015.12.103.

[6] J.H. Kim, M.G. Lee, D. Kim, D.K. Matlock, R.H. Wagoner, Hole-expansion formability of dual-phase steels using representative volume element approach with boundary-smoothing technique, *Mater. Sci. Eng. A.* **527** (2010) 7353–7363. https://doi.org/10.1016/j.msea.2010.07.099.

[7] M. Calcagnotto, Y. Adachi, D. Ponge, D. Raabe, Deformation and fracture mechanisms in fine- and ultrafine-grained ferrite/martensite dual-phase steels and the effect of aging, *Acta Mater*. **59** (2011) 658–670. https://doi.org/10.1016/j.actamat.2010.10.002.

[8] M. Calcagnotto, D. Ponge, D. Raabe, Effect of grain refinement to 1μm on strength and toughness of dual-phase steels, *Mater. Sci. Eng. A.* **527** (2010) 7832–7840. https://doi.org/10.1016/j.msea.2010.08.062.

[9] D. Terada, G. Ikeda, M.-H. Park, A. Shibata, N. Tsuji, Reason for high strength and good ductility in dual phase steels composed of soft ferrite and hard martensite, *in: IOP Conf. Ser. Mater. Sci. Eng.*, 2017. https://doi.org/10.1088/1757-899X/219/1/012008.

[10] K. Park, M. Nishiyama, N. Nakada, T. Tsuchiyama, S. Takaki, Effect of the martensite distribution on the strain hardening and ductile fracture behaviors in dual-phase steel, *Mater. Sci. Eng. A.* **604** (2014) 135–141. https://doi.org/10.1016/j.msea.2014.02.058.

[11] M. Soliman, H. Palkowski, Tensile properties and bake hardening response of dual phase steels with varied martensite volume fraction, *Mater. Sci. Eng. A.* **777** (2020) 139044. https://doi.org/10.1016/j.msea.2020.139044.

[12] Y. Il Son, Y.K. Lee, K.T. Park, C.S. Lee, D.H. Shin, Ultrafine grained ferrite-martensite dual phase steels fabricated via equal channel angular pressing: Microstructure and tensile properties, *Acta Mater.* **53** (2005) 3125–3134. https://doi.org/10.1016/j.actamat.2005.02.015.

[13] H. Li, S. Gao, Y. Tian, D. Terada, A. Shibata, N. Tsuji, Influence of Tempering on Mechanical Properties of Ferrite and Martensite Dual Phase Steel, *Mater. Today Proc.* **2** (2015) S667–S671. https://doi.org/10.1016/j.matpr.2015.07.372.

[14] K. Ismail, A. Perlade, P.J. Jacques, T. Pardoen, L. Brassart, Impact of second phase morphology and orientation on the plastic behavior of dual-phase steels, *Int. J. Plast.* **118** (2019) 130–146. https://doi.org/10.1016/j.ijplas.2019.02.005.

[15] M. Jafari, S. Ziaei-Rad, N. Saeidi, M. Jamshidian, Micromechanical analysis of martensite distribution on strain localization in dual phase steels by scanning electron microscopy and crystal plasticity simulation, *Mater. Sci. Eng. A.* **670** (2016) 57–67. https://doi.org/10.1016/j.msea.2016.05.094.

[16] C.C. Tasan, J.P.M. Hoefnagels, M. Diehl, D. Yan, F. Roters, D. Raabe, Strain localization and damage in dual phase steels investigated by coupled in-situ deformation experiments and crystal plasticity simulations, *Int. J. Plast.* **63** (2014) 198–210. https://doi.org/10.1016/j.ijplas.2014.06.004.

[17] V. Herrera-Solaz, L. Patriarca, S. Foletti, J. Segurado, M. Niffenegger, Microstructure-based modelling and Digital Image Correlation measurement of strain fields in austenitic stainless steel 316L during tension loading, *Mater. Sci. Eng. A.* **751** (2019) 99–106. https://doi.org/10.1016/j.msea.2019.02.063.

[18] S.H. Joo, J.K. Lee, J.M. Koo, S. Lee, D.W. Suh, H.S. Kim, Method for measuring nanoscale local strain in a dual phase steel using digital image correlation with nanodot patterns, *Scr. Mater.* **68** (2013) 245–248. https://doi.org/10.1016/j.scriptamat.2012.10.025.

[19] Y.F. Wang, C.X. Huang, X.T. Fang, H.W. Höppel, M. Göken, Y.T. Zhu, Hetero-deformation induced (HDI) hardening does not increase linearly with strain gradient, *Scr. Mater.* **174** (2020) 19–23. https://doi.org/10.1016/j.scriptamat.2019.08.022.

[20] F. Briffod, H. Hu, T. Shiraiwa, M. Enoki, Effect of in-lath slip strength on the strain

partitioning in a dual-phase steel investigated by high-resolution digital image correlation and crystal plasticity simulations, Mater. Sci. Eng. A. 862 (2023) 144413. https://doi.org/10.1016/j.msea.2022.144413.

[21] D. Yan, C.C. Tasan, D. Raabe, High resolution in situ mapping of microstrain and microstructure evolution reveals damage resistance criteria in dual phase steels, Acta Mater. 96 (2015) 399–409. https://doi.org/10.1016/j.actamat.2015.05.038.

[22] M. Azuma, S. Goutianos, N. Hansen, G. Winther, X. Huang, Effect of hardness of martensite and ferrite on void formation in dual phase steel, *Mater. Sci. Technol. (United Kingdom).* **28** (2012) 1092–1100. https://doi.org/10.1179/1743284712Y.0000000006.

[23] Q. Han, A. Asgari, P.D. Hodgson, N. Stanford, Strain partitioning in dual-phase steels containing tempered martensite, *Mater. Sci. Eng. A.* **611** (2014) 90–99. https://doi.org/10.1016/j.msea.2014.05.078.

[24] E.E. Aşık, E.S. Perdahcıoğlu, A.H. van den Boogaard, Microscopic investigation of damage mechanisms and anisotropic evolution of damage in DP600, *Mater. Sci. Eng. A.* **739** (2019) 348–356. https://doi.org/10.1016/j.msea.2018.10.018.

[25] H. Toda, A. Takijiri, M. Azuma, S. Yabu, K. Hayashi, D. Seo, M. Kobayashi, K. Hirayama, A. Takeuchi, K. Uesugi, Damage micromechanisms in dual-phase steel investigated with combined phase- and absorption-contrast tomography, *Acta Mater.* **126** (2017) 401–412. https://doi.org/10.1016/j.actamat.2017.01.010.

[26] J. Kadkhodapour, A. Butz, S. Ziaei Rad, Mechanisms of void formation during tensile testing in a commercial, dual-phase steel, *Acta Mater.* **59** (2011) 2575–2588. https://doi.org/10.1016/j.actamat.2010.12.039.

[27] M.H. Park, A. Shibata, N. Tsuji, Grain refinement of 2Mn-0.1C steel by repetitive heat treatment and recrystallization, i*n: IOP Conf. Ser. Mater. Sci. Eng.*, 2015. https://doi.org/10.1088/1757-899X/89/1/012041.

[28] M. Park, A. Shibata, N. Tsuji, Challenging Ultra Grain Refinement of Ferrite in Low-C Steel Only by Heat Treatment, *Front. Mater.* **7** (2020) 1–10. https://doi.org/10.3389/fmats.2020.604792.

[29] A. Shibata, T. Nagoshi, M. Sone, S. Morito, Y. Higo, Evaluation of the block boundary and sub-block boundary strengths of ferrous lath martensite using a micro-bending test, *Mater. Sci. Eng. A.* **527** (2010) 7538–7544. https://doi.org/10.1016/j.msea.2010.08.026.

[30] T. Kaneshita, G. Miyamoto, T. Furuhara, Variant selection in grain boundary nucleation of bainite in Fe-2Mn-C alloys, *Acta Mater.* **127** (2017) 368–378.

https://doi.org/10.1016/j.actamat.2017.01.035.

[31] S. Morito, H. Yoshida, T. Maki, X. Huang, Effect of block size on the strength of lath martensite in low carbon steels, *Mater. Sci. Eng. A.* **438–440** (2006) 237–240. https://doi.org/10.1016/j.msea.2005.12.048.

[32] T. Tomida, Variant selection mechanism by elastic anisotropy and double K-S relation for transformation texture in steel; difference between martensite and ferrite, *Acta Mater*. **146** (2018) 25–41. https://doi.org/10.1016/j.actamat.2017.12.033.

[33] A. Considère, *Ann. Ponts Chaussees* **9** (1885) 574-775.